

OBSERVATIONAL SIGNATURES OF END-DOMINATED COLLAPSE IN THE S242 FILAMENTARY STRUCTURE

L. K. DEWANGAN¹, L. E. PIROGOV², O. L. RYABUKHINA^{2,3}, D. K. OJHA⁴, AND I. ZINCHENKO²

ABSTRACT

We present new CO (¹³CO(1–0) and C¹⁸O(1–0)) and CS(2–1) line observations of an elongated filamentary structure (length ~ 30 pc) in the star-forming site S242, which were taken with the OSO-20m telescope. One filament’s end hosts the S242 H II region, while the other end contains *Planck* cold clumps. Several sub-regions are identified in the filament, and are supersonic with Mach number of 2.7–4.0. The study of the dynamical states shows supercritical nature of the sub-regions (except central part), which could not be supported by a combination of thermal and turbulent motions. Young stellar objects are seen toward the entire filament, but more concentrated toward its ends. Dense molecular cores are observed mainly toward the filament ends, and are close to virial equilibrium. Position-velocity plots trace velocity gradients ($\sim 1 \text{ km s}^{-1} \text{ pc}^{-1}$) toward both the ends. An oscillatory pattern in velocity is also observed toward the filament, indicating its fragmentation. The collapse timescale of the filament is computed to be ~ 3.5 Myr. Using the ¹³CO data, the structure function in velocity of the filament is found to be very similar as seen in the Musca cloud for lags ~ 1 – 3 pc, and deviates from the Larson’s velocity-size relationship. The observed oscillatory pattern in the structure function at higher lags suggests the existence of large-scale and ordered velocity gradients as well as the fragmentation process through accretion along the filament. Considering all the observed results along with their uncertainties, the S242 filament is a very good example of the end-dominated collapse.

Subject headings: dust, extinction – HII regions – ISM: clouds – ISM: individual object (S242) – stars: formation – stars: pre-main sequence

1. INTRODUCTION

In the past fifteen years, there has been a remarkable observational progress in the study of star formation with the availability of the infrared and sub-millimeter (sub-mm) data provided by the space-based *Spitzer* and *Herschel* telescope facilities (e.g., Churchwell et al. 2006, 2007; André et al. 2010, 2014). These data sets have unveiled numerous filamentary features, where mid-infrared bubbles/shells associated with H II regions, embedded clumps, and clusters of young stellar objects (YSOs) are commonly identified (e.g., Deharveng et al. 2010; André et al. 2014). These observational evidences have encouraged investigators to study the physical mechanisms of filament fragmentation, and the role of filaments in the formation of dense massive star-forming clumps and young stellar clusters (e.g., Myers 2009; André et al. 2010; Deharveng et al. 2010; Schneider et al. 2012; Baug et al. 2015; Dewangan et al. 2015, 2016a,b, 2017a,b,c,d,e; Contreras et al. 2016), which are still debated. In this context, some existing models for the long, but finite-sized, filaments predict that the fragmentation and collapse can take place at the ends of the filaments (i.e., end-dominated collapse), where the gas has an enhanced acceleration (e.g., Bastien 1983; Burkert & Hartmann 2004; Heitsch et al. 2008; Pon et al. 2011, 2012; Clarke &

Whitworth 2015). However, observational assessment of such existing numerical simulations is very limited in the literature (e.g., Zernickel et al. 2013; Beuther et al. 2015; Kainulainen et al. 2016; Hacar et al. 2016). It requires a promising sample of the filamentary features and the knowledge of molecular gas motion in the direction of these objects (e.g., Kainulainen et al. 2016; Contreras et al. 2016; Williams et al. 2018). However, high-resolution molecular line observations of several interesting filamentary features revealed by the space-based telescopes are not available. In this connection, an embedded filamentary structure in a massive star-forming region, LBN 182.30+00.07 or Sh 2-242 (hereafter S242) can be considered as one of such sources (e.g., Dewangan et al. 2017c, hereafter Paper I), and is the target source of the present study. To examine the dynamics and physical conditions of the gas in the S242 filament, an extensive analysis of new molecular (CO and CS) line observations taken with the 20-m telescope of the Onsala Space Observatory (OSO) is carried out in this paper. Such investigation has also allowed us to examine the existing numerical predictions concerning the fragmentation of filamentary feature.

Following the introduction in this section, we give an overview of the site S242 in Section 2. In Section 3, we present the molecular line observations and data reduction. Observational outcomes are presented in Section 4, and are discussed in Section 5. The main conclusions of this paper are summarized in Section 6.

2. OVERVIEW OF THE SITE S242

Situated at a distance of 2.1 ± 0.7 kpc (Blitz et al. 1982), the site S242 is associated with a filamentary structure, which has been revealed by the *Herschel* sub-mm data (e.g., Paper I). Based on the published results from Pa-

lokeshd@prl.res.in

¹ Physical Research Laboratory, Navrangpura, Ahmedabad - 380 009, India.² Institute of Applied Physics of the Russian Academy of Sciences, 46 Ulyanov st., Nizhny Novgorod 603950, Russia.³ Institute of Astronomy of the Russian Academy of Sciences, 48 Pyatnitskaya st., Moscow 119017, Russia.⁴ Department of Astronomy and Astrophysics, Tata Institute of Fundamental Research, Homi Bhabha Road, Mumbai 400 005, India.

per I, Figures 1a and 1b display the *Herschel* column density and temperature maps (resolution $\sim 37''$) of the site S242, respectively. A variation in the dust temperature is evident along the major axis of the filament (see Figure 1b). The locations of the ionized emission traced in the NVSS 1.4 GHz continuum map are found in Figure 1b. The southern end of the filament has been found to host the S242 HII region, where an extended structure in the *Herschel* temperature map is depicted with a temperature (T_d) range of ~ 19 – 26 K (see Figure 1b). The S242 HII region was found to be powered by a star BD+26 980 of spectral type B0.5V–B0V (Hunter & Massey 1990), and has a dynamical age of ~ 0.5 Myr (see also Paper I). In Paper I, the photometric 1 – 5 μm data of point-like sources were analyzed to identify YSOs in the site S242, which are also shown in Figure 1c. Both the northern and southern ends of the S242 filament have been found with the noticeable star formation activities compared to its other parts (see Figure 1c). In the southern direction, a molecular CO outflow toward IRAS 05490+2658, which is situated $\sim 5'$ east of the S242 HII region, was reported by Snell et al. (1990) (see also Varricatt et al. 2010). Several *Herschel* clumps/condensations have been identified along the filament (see Figure 1a). The most massive clumps ($M_{clump} \sim 250$ – $1020 M_\odot$) have also been detected toward both the filament ends (see Table 1 in Paper I). It was also found that the total mass of three *Herschel* clumps (i.e. $\sim 1700 M_\odot$) seen in the southern filament end was almost equal to the total mass of three clumps (i.e. $\sim 1750 M_\odot$) observed in the northern filament end (see Table I in Paper I). Based on the NANTEN $^{13}\text{CO}(1-0)$ low-resolution map (beam size $\sim 2'.7$), molecular gas toward the site S242, having a radial velocity (V_{lsr}) of ~ 0.7 km s^{-1} , was studied by Kawamura et al. (1998). To the best of our knowledge, there are no high-resolution molecular line observations reported toward the S242 filament. In Paper I, the observed results in the site S242 were explained by the end-dominated collapse process. However, the study related to the internal dynamical properties/internal kinematics of the emitting gas in the filament is yet to be performed, which is essential to further explore the ongoing physical process in the site S242.

3. DATA AND ANALYSIS

3.1. New Observations

New molecular line observations were carried out in March 2018 with the 20-m telescope of the OSO (project O2017a-03). We used the 3-mm dual-polarization receiver with a SIS mixer, which has a noise temperature of ~ 45 – 60 K in the 85–116 GHz frequency range (Belitsky et al. 2015). Fast Fourier Transform spectrum analyser with a 2.5 GHz bandwidth and a 76 kHz frequency resolution (32768 channels) was used in the observational experiment. The CO ($^{13}\text{CO}(1-0)$ and $\text{C}^{18}\text{O}(1-0)$) and CS(2–1) lines were simultaneously observed in the upper (i.e. 110 GHz) and lower (i.e. 98 GHz) sidebands, respectively. The spectrometer gives a velocity resolution of ~ 0.21 – 0.23 km s^{-1} at these frequencies. To obtain high sensitivity data, the signals from two polarizations were added during the reduction process, which provided an increase of sensitivity by a factor of $\sqrt{2}$. Observations were performed in the frequency switching mode.

The system noise temperature during most of the observations varied in ranges of ~ 160 – 300 K (at 110 GHz) and ~ 115 – 200 K (at 98 GHz) depending on the elevation of the target. Main beam efficiency depends on the source elevation, and varies in the ranges of ~ 0.32 – 0.45 (at 110 GHz) and 0.38 – 0.50 (at 98 GHz) for elevations of $\sim 25^\circ$ – 60° . These parameters were used to convert antenna temperatures to main beam brightness temperatures. The half power beam widths of the OSO-20m antenna are $\sim 35''$ (at 110 GHz) and $\sim 39''$ (at 98 GHz). Pointing and focus were regularly checked by the observations of SiO masers. Mapping was done with $20''$ grid spacing. The line data were processed using the CLASS program from the GILDAS¹ package, the XS software², and our original programs.

3.2. Others

The archival data sets in the radio and sub-mm regimes were obtained from publicly available surveys (e.g., the NRAO VLA Sky Survey (NVSS; $\lambda = 21$ cm; resolution = $45''$; Condon et al. 1998), *Planck*³ intensity image ($\lambda = 850$ μm ; resolution = $300''$; *Planck Collaboration IX 2014*) observed with the High Frequency Instrument (HFI) at 353 GHz, and the *Herschel* Infrared Galactic Plane Survey (Hi-GAL; $\lambda = 70, 160, 250, 350, 500$ μm ; resolutions = $5''.8, 12'', 18'', 25'', 37''$; Molinari et al. 2010)). We also used the published results from Paper I.

4. RESULTS

4.1. S242 site: *Planck* Galactic Cold Clumps

In the direction of the northern filament end, at least five *Planck* Galactic Cold Clumps (PGCCs; from Yuan et al. 2016) are reported (see Figure 1a). It is thought that PGCCs may represent the early stages of star formation (e.g., Tang et al. 2018). Using the HCN ($J = 1-0$) and HCO^+ ($J = 1-0$) line observations, Yuan et al. (2016) studied dense gas toward the PGCCs in a velocity (V_{lsr}) range of 1.95 – 2.2 km s^{-1} . The positions of PGCCs G181.84+00.31a1, G181.84+00.31a2, G181.84+00.31b1, G181.84+00.31b2, and G182.04+00.41b1 are shown in Figure 1a (see Yuan et al. 2016, for more details).

We find a radio continuum source NVSS 055101+273627 (e.g., Condon et al. 1998) toward the PGCC G181.84+00.31a1 (see an arrow in Figures 1a and 1b), while other remaining PGCCs are not associated with the NVSS radio continuum emission ($1\sigma \sim 0.45$ mJy beam $^{-1}$). Using the NVSS radio continuum data, the source NVSS 055101+273627 is found to be powered by a B1V–B0.5V type star, and its dynamical age is estimated to be ~ 0.1 Myr. In Figure 1c, a majority of the YSOs are found toward both the filament ends (i.e., the S242 HII region and PGCCs). The clumps traced in the southern filament end containing the S242 HII region are found with relatively the warm dust emission

¹ <http://www.iram.fr/IRAMFR/GILDAS>

² <https://www.chalmers.se/en/researchinfrastructure/oso/radioastronomy/Pages/software.aspx>

³ *Planck* (<http://www.esa.int/Planck>) is a project of the European Space Agency (ESA) with instruments provided by two scientific consortia funded by ESA member states and led by Principal Investigators from France and Italy, telescope reflectors provided through a collaboration between ESA and a scientific consortium led and funded by Denmark, and additional contributions from NASA (USA).

compared to the clumps observed in the northern filament end hosting the PGCCs (see Figure 1b). It seems that the clumps distributed toward both the filament ends are probably at different evolutionary stages.

4.2. S242 site: Spatial distribution of molecular gas

Figure 2 shows an intensity map of $^{13}\text{CO}(1-0)$ integrated over a velocity interval of $[-12, 6]$ km s^{-1} . Interestingly, the elongated appearance of filamentary feature in the site S242, having length ~ 30 pc, is traced in the molecular map as seen in the *Herschel* column density map (see Figure 1a). Several molecular condensations in the filament can also be identified in Figure 2. The IRAS sources located toward both the filament ends are also shown in Figure 2.

We have also presented integrated intensity (moment-0) maps of $^{13}\text{CO}(1-0)$, $\text{C}^{18}\text{O}(1-0)$, and $\text{CS}(2-1)$ emission in Figures 3a, 3b, and 3c, respectively. The ^{13}CO moment-0 map is shown here only for comparison (see also Figure 2). The C^{18}O line is a tracer of total molecular gas column density, while the CS line is known to depict denser molecular gas compared to the ^{13}CO data. Hence, the denser parts in the filament can be spatially examined in Figures 3b and 3c. The dense gas traced in the $\text{C}^{18}\text{O}(1-0)$ and $\text{CS}(2-1)$ maps is found toward both the filament ends (i.e. the S242 H II region and all the PGCCs). Figures 3d, 3e, and 3f show moment-1 (velocity field) maps of the $^{13}\text{CO}(1-0)$, $\text{C}^{18}\text{O}(1-0)$, and $\text{CS}(2-1)$, respectively. With the help of moment-1 map, some signatures of velocity gradients are seen at both the ends of the filament (see Figure 3d).

Figures 4 and 5 display the ^{13}CO and $\text{CS}(2-1)$ velocity channel maps from -1 to 5 km s^{-1} , respectively. Each channel map is obtained by integrating the emission over 1 km s^{-1} velocity intervals. These channel maps help us to examine the gas distribution in the filament for a given velocity interval. In this paper, the molecular gas in the filament is mainly studied in the velocity interval of $[-1, 5]$ km s^{-1} . However, we find an additional velocity component at $[-12, -6]$ km s^{-1} toward the northern part of the filament using the ^{13}CO line data (not shown in this paper). In this velocity range, there is no $\text{C}^{18}\text{O}(1-0)$ and $\text{CS}(2-1)$ emission detected toward the filament. It implies that the gas at $[-12, -6]$ km s^{-1} has low density. In the position-velocity (pv) plot, we find that the velocity component at $[-12, -6]$ km s^{-1} is kinematically unrelated to the one at the $[-1, 5]$ km s^{-1} (not shown in this paper). Furthermore, the emission at $[-12, -6]$ km s^{-1} appears to be more extended to the north of the filament, which is not covered in this observational work. In order to make any further conclusion on the kinematical structure at $[-12, -6]$ km s^{-1} , one needs to obtain further observations for a wide-scale area containing the north part of the filament.

In Figure 6a, an arbitrarily chosen solid curve is highlighted on the integrated intensity map of ^{13}CO emission, where the pv, V_{lsr} , and ΔV plots are calculated (see Figures 7a, 7b, and 9). The curve indicates the major axis of the filament, and is seen in the direction of the S242 H II region, the northern cluster of YSOs, and the positions of IRAS 05483+2728 and IRAS 05490+2658 (see Figures 1c and 2).

4.2.1. Sub-regions in S242 site

According to the visual analysis of the ^{13}CO intensity map, several sub-regions are outlined for computing the molecular gas masses (see Figure 6b). We have used the optically thin C^{18}O line data to compute the mass of each selected sub-region in the S242 site. Masses (M_{subreg}) are obtained by integrating the column density $N(\text{H}_2)$ over the outlined sub-regions (see Figure 6b) and multiplying by $2.8 \times m_H$, where m_H is the hydrogen atom mass. To obtain $N(\text{H}_2)$, we have calculated $N(\text{C}^{18}\text{O})$ from the C^{18}O integrated intensities in the optically thin and the local thermodynamic equilibrium (LTE) approximations using an expression from Mangum & Shirley (2016), which is given by

$$N(\text{C}^{18}\text{O}) = \frac{2.48 \times 10^{14} (T_{ex} + 0.88) \exp\left(\frac{5.27}{T_{ex}}\right)}{\exp\left(\frac{5.27}{T_{ex}}\right) - 1} \times \left[\frac{\int T_R dv (\text{km s}^{-1})}{f (J_\nu(T_{ex}) - J_\nu(T_{bg}))} \right] \text{cm}^{-2} \quad (1)$$

where T_{ex} is the excitation temperature which is adopted to be 10 K, f ($= 1$) is the main beam filling factor (i.e., the fraction of the spatial resolution of the measurement filled by the source), T_{bg} ($= 2.73$ K) is the cosmic background temperature, $J(T) = \frac{h\nu}{k} / (\exp(\frac{h\nu}{kT}) - 1)$, h is the Planck constant, $\int T_R dv$ is the integral over the line profile. Considering a column density ratio $[\text{C}^{18}\text{O}]/[\text{H}_2]$ equal to 1.7×10^{-7} (Frerking et al. 1982), the values of $N(\text{H}_2)$ are calculated. The values of M_{subreg} and length of sub-regions are tabulated in Table 1. These values also allow us to estimate the observed line mass ($M_{\text{line,obs}}$) of each sub-region (see Table 1).

We have also obtained the critical line mass ($M_{\text{line,crit}}$) of a filament. For the case of an infinite, isothermal cylinder in equilibrium between thermal and gravitational pressures, the expression of $M_{\text{line,crit}}$ (Ostriker 1964) is equal to $2c_s^2/G \sim 16 M_\odot \text{pc}^{-1} \times (T/10 \text{ K})$; where c_s is the isothermal sound speed at $T(\text{K})$ and G is the gravitational constant. The contribution of the non-thermal microturbulent gas motions can be included in the calculation of the critical line mass, which is also known as the virial line mass (i.e., André et al. 2014; Kainulainen et al. 2016). In order to obtain the expression of the virial line mass (i.e. $M_{\text{line,vir}} = 2c_{s,\text{eff}}^2/G$; André et al. 2014; Kainulainen et al. 2016), the sound speed is replaced by an effective sound speed ($c_{s,\text{eff}} = (c_s^2 + \sigma_{\text{NT}}^2)^{1/2}$; where σ_{NT} is the non-thermal velocity dispersion) in the equation of the critical line mass. We can further write the expression of the virial line mass as:

$$M_{\text{line,vir}} = \left[1 + \left(\frac{\sigma_{\text{NT}}}{c_s} \right)^2 \right] \times \left[16 M_\odot \text{pc}^{-1} \times \left(\frac{T}{10 \text{ K}} \right) \right] \quad (2)$$

The non-thermal velocity dispersion is defined by:

$$\sigma_{\text{NT}} = \sqrt{\frac{\Delta V^2}{8 \ln 2} - \frac{kT_{kin}}{30m_H}} = \sqrt{\frac{\Delta V^2}{8 \ln 2} - \sigma_T^2}, \quad (3)$$

where ΔV is the measured Full Width Half Maximum (FWHM) linewidth of the observed C^{18}O spectra, T_{kin}

is the gas kinetic temperature (i.e. 10 K), and σ_T ($= (kT_{kin}/30m_H)^{1/2}$) is the thermal broadening for $C^{18}O$ at T_{kin} . Mach number (i.e. ratio of σ_{NT}/c_s) is also estimated for each sub-region, where c_s is defined earlier ($c_s = (kT_{kin}/\mu m_H)^{1/2} = 0.19 \text{ km s}^{-1}$ for $T_{kin} = 10 \text{ K}$ and mean molecular weight (μ) = 2.33). The observed Mach number range is computed to be 2.7–4.0, indicating that all the sub-regions are supersonic. Table 1 also lists the linewidth (ΔV ($C^{18}O$)), σ_{NT} , and $M_{line,vir}$ of each sub-region.

The uncertainties of the observed line masses mainly depend on the uncertainty of distance to S242 ($\sim 30\%$; Blitz et al. 1982). The adopted value of the excitation temperature ($T_{ex} = 10 \text{ K}$) could also affect the values of $N(C^{18}O)$. If we adopt the lower T_{ex} ($= 5 \text{ K}$) or higher T_{ex} ($= 20 \text{ K}$) in the calculation then the line mass is computed to be about 1.2–1.4 times the one at $T_{ex} = 10 \text{ K}$. Here, one may also keep in mind that the $[C^{18}O]/[H_2]$ ratio for S242 could be about 1.5 times low due to the $[^{16}O]/[^{18}O]$ dependence on galactocentric distance (e.g., Wilson & Rood 1994). Hence, due to these factors, the observed line mass estimates could be underestimated twice.

The uncertainties of virial line masses depend on the value of mean gas kinetic temperature of sub-regions ($\sim 10 \text{ K}$) and the uncertainties of $C^{18}O$ FWHM. The uncertainties of $C^{18}O$ FWHM calculated from the Gaussian fits lead to the uncertainties of ~ 4 – 14% in $M_{line,vir}$. In the direction of the S242 H II region/sub-region 1, the dust temperature (T_d) range is found to be ~ 19 – 26 K (see Figure 1b). If we choose $T_{kin} = 20 \text{ K}$ in the calculation of $M_{line,vir}$ then it leads the uncertainty of $\sim 10\%$ in $M_{line,vir}$. Note that the observed line masses and virial line masses are calculated with an assumption of a zero inclination of the filament, which is unknown. Hence, these both observed values represent upper limits. Taking into account these considerations, it is possible to state that the observed line masses (mass-to-length ratios) of different parts of the S242 filament are systematically higher than $M_{line,vir}$, implying that these sub-regions (except sub-region “2” or central part of the filament) could be unstable (see Table 1).

Furthermore, using the CS(2-1) and $C^{18}O$ maps, at least five dense cores are selected in the filament. These cores are indicated by ellipses on the CS(2-1) map (Figure 6c). The deconvolved mean size of each ellipse is also computed by the Gaussian fitting (see Pirogov et al. 2003). Two compact cores (sizes ~ 0.8 – 0.9 pc) are located near the H II region in the direction of the southern filament end. A dense core “3” (size $\sim 1.3 \text{ pc}$; see Figure 6c) in the northern part of the filament seems to be associated with PGCC G182.04+0042b1. The observed cores are also associated with the *Herschel* clumps of higher sizes (see Paper I). A dense core (see ID “5” in Figure 6c) is also embedded in the sub-region “3”. The masses of the cores derived from the $C^{18}O(1-0)$ integrated intensities are ~ 250 – $350 M_\odot$. We have also computed the virial mass ($M_{vir} (M_\odot) = k D_c \Delta V^2$; MacLaren et al. 1988, where the parameter $k = 105$ for spherically-symmetric core/clump/cloud with constant density, no external pressure, and no magnetic fields) of diameter D_c (in pc) and linewidth ΔV (in km s^{-1}). Table 2 contains the derived physical parameters of the cores (i.e.,

position, diameter (D_c), mass (M_c), linewidth ($CS \Delta V$), M_{vir} , and mean volume density (\bar{n}). The cores “1” and “2” located near the S242 H II region have mean densities several times higher than that of the northern cores “3–5”. The uncertainties of the core masses also depend on the uncertainties of distance to S242, $[C^{18}O]/[H_2]$ ratio, CS FWHM, sizes derived from the Gaussian fits, and excitation temperature. Considering all these factors, the uncertainties of the virial masses of the cores lie in the range of ~ 30 – 60% . Taking into account the uncertainties of virial mass calculations, the core mass estimates are considered to be close to virial ones, which are typical for star-forming cores.

Note that the sub-region “3” contains a dense core and noticeable YSOs, revealing an ongoing star formation in this sub-region. However, the sub-region “3” appears away from the major axis of the filamentary structure (see Figures 1a and 6b). Hence, we have not further discussed the results of this particular sub-region in this paper.

4.3. Position-velocity plots

4.3.1. Velocity field

In order to study the velocity structure of molecular gas in our selected target, the pv maps of ^{13}CO and $C^{18}O$ emission are shown in Figures 7a and 7b, respectively. These maps are extracted along the major axis of the filament (see Figure 6a). Both the pv maps reveal an oscillatory-like velocity pattern along the filament, which is more prominently seen in Figure 7b (see a dashed curve in Figure 7b). Interestingly, velocity gradients ($\sim 1 \text{ km s}^{-1} \text{ pc}^{-1}$) are also observed in the direction of the both filament ends, where velocity oscillations are quite large compared to other parts. Furthermore, the velocity spread (i.e., -1 to 4 km s^{-1}) is also very high in the direction of the S242 H II region or IRAS 05490+2658. Previously, Snell et al. (1990) found a molecular CO outflow toward IRAS 05490+2658 (see Figure 11 in their paper).

In Figure 8, we present plots of velocity scans nearly perpendicular to the filament for different $\Delta\delta$ values (see also Figure 2). In several panels in Figure 8, one can find signatures of the oscillatory-like velocity pattern, and the velocity is more or less constant in some panels. Figures 9a and 9b display a variation of $^{13}CO V_{lsr}$ and ΔV against the major axis of the filament, respectively. In order to produce these figures, we analyzed the spectra, where the ^{13}CO integrated intensities are higher than 3σ . Based on a visual inspection of the total spectral map, emission region was divided into subzones. For each subzone, the spectra were fitted with one or two Gaussian functions. An initial guess of line parameters was taken from averaged spectra over the subzones. Figures 9c and 9d show a variation of CS(2-1) V_{lsr} and CS(2-1) integrated intensity against the major axis of the filament, respectively. In Figure 9, all the points are obtained from the averaging of 9 spectra over the same bins.

We have fitted the Gaussian profile(s) to the observed individual spectrum to model line shape, which enables us to infer the value of radial velocity ($^{13}CO V_{lsr}$) and linewidth ($^{13}CO \Delta V$). Figure 10 shows three ^{13}CO spectra at different positions, which are also superimposed with the Gaussian profiles. The ^{13}CO line profiles in

the main part of the filament (i.e., $\sim -700'' < \Delta\delta < \sim 1000''$) are often double-peaked. The $\text{C}^{18}\text{O}(1-0)$ profiles also show double-peaked behaviour as seen in the ^{13}CO line profiles, implying superposition of at least two closely located velocity components instead of systematic motions. In many cases, two components are clearly separated by 1 km s^{-1} , where two Gaussian functions were fitted to the spectra (see Figure 10). In the remaining cases, a single Gaussian fitting was performed. The component with lower velocity corresponds to the main velocity component of the filament.

In Figure 9a, we have plotted main velocity component with dark blue squares, while the second velocity component is drawn with light blue squares. The FWHM of the main component (ΔV) against the major axis of the filament is shown in Figure 9b. An oscillatory-like pattern with a period of $\sim 6\text{--}10 \text{ pc}$ is seen in both the figures. In Figure 9d, there are two peaks seen prominently, which correspond to the cores “1” and “3”, respectively. It seems that an oscillatory pattern in $\text{CS}(2-1) V_{lsr}$ could be connected with the fragmentation at the ends of the filament, while in the case of the central part, the $\text{CS}(2-1)$ data of higher quality is needed to make definite conclusions related to the link of velocity oscillations with fragmentation (see Figures 9c and 9d).

The implication of all these results are discussed in Section 5.

4.3.2. Structure function in velocity

In Section 4.2.1, we find that the observed linewidths are much higher than the thermal ones, implying that the non-thermal (such as turbulent motions) could be responsible for the line broadening in the filament. With the help of our ^{13}CO line data, it is possible to employ statistical methods for analyzing the properties of turbulence in our selected target. The studies of turbulence in molecular clouds usually use the dependence between molecular linewidths and cloud sizes. In this connection, in the literature, we find the Larson’s one-dimensional velocity dispersion-size relationship with $\delta V = 0.63 \times L^{0.38}$, which was obtained for a range of cloud sizes of $\sim 0.1\text{--}100 \text{ pc}$ (Larson 1981). Using more homogeneous data sets, Solomon et al. (1987) corrected the slope of the Larson’s dependence to be 0.5. Later, velocity structure functions of individual sample clouds derived by Heyer & Brunt (2004) were appeared to be nearly identical to Larson’s $\delta V\text{--}L$ dependence, indicating that it has its origin in turbulence properties. For the Musca cloud, Hacar et al. (2016) derived velocity structure function using the ^{13}CO data, and found significant departures from the Larson’s law. They explained this deviation by the existence of sonic-like structures in the cloud decoupled from the supersonic turbulent regime.

Following the analysis presented in Hacar et al. (2016), we calculated the reframed/second-order structure function ($S_2(L)$) using the ^{13}CO main velocity component (see blue points in Figure 9a), and the square root of the second-order structure function is given by:

$$S_2(L)^{1/2} = \delta V = \langle |V(r) - V(r+L)|^2 \rangle^{1/2} \quad (4)$$

In the calculations, the ^{13}CO integrated intensities ($I(^{13}\text{CO}(1-0)) \geq 2 \text{ K km s}^{-1}$) are adopted, and a total number of the data points are found to be 2346. The

total range of angular distances ($\sim 20'' - 3170''$) between two positions is divided into subranges (or lags) of $20''$ width ($\sim 0.2 \text{ pc}$ in linear scale). For each lag, the value of structure function in velocity (i.e., δV) is calculated. The error of the structure function for a given lag was calculated by individual errors of line velocities obtained from the Gaussian fits and by the method of error propagation. It is found to be $\lesssim 0.001 \text{ km s}^{-1}$ for the most cases. The result concerning the structure function in velocity calculated for the total data set is shown in Figure 11, where angular distances are converted into linear ones (L). For $L \lesssim 3 \text{ pc}$, we find a power-law behavior (i.e., $\delta V = 0.42 \times L^{0.48}$; see a solid black line in Figure 11). The uncertainties of the regression line parameters are small, and the correlation coefficient is close to unity. This observed dependence lies lower than the Larson’s dependence (see a broken line (in blue) in Figure 11). However, the observed slope in this study is close to the one found by Solomon et al. (1987). Furthermore, the behavior of δV against length (lag) (or the structure function) is very similar to those found for the Musca cloud in a range of $L \sim 1\text{--}3 \text{ pc}$ (see Figure 5 in Hacar et al. 2016) (see a broken line (in red) in Figure 11). For larger distances ($L > 3 \text{ pc}$), the structure function rises, and has an oscillatory behavior. We have calculated the structure function excluding the regions of active star formation (i.e., the northern and southern filament ends), however we do not find any difference from the result obtained for the total data set. We have also made a comparison of our outcomes with the published results of the Musca cloud (Hacar et al. 2016) and, have found no prominent deviation from the single power-law dependence at lower lags.

The results related to the structure function apparently depend on the inclination effect. If the filament has non-zero inclination then the projection of the linear distance between two points, which is collinear to the projection of the filament’s axis, will be increased by a factor of $1/\cos(i)$, where “ i ” is an inclination angle. This will cause stretching of the structure function compared to the case of a zero inclination. The stretching is expected to be non-uniform. For the lags much larger than the filament’s width, the projections of the distances between two points will be nearly collinear to the projection of the filament’s axis. For small lags, an averaging will go over projections with different angles with respect to the projection of the filament’s axis, and the stretching will be lower. However, even in this case, the stretching will take place, and a slope of the regression line calculated for the range of small lags will be lower than in the case of a zero inclination. To obtain the precise estimates, a detailed modelling is needed.

We have also calculated the structure functions for different sub-regions as outlined in Figure 6b. For small lags ($\lesssim 2\text{--}3 \text{ pc}$), the structure functions of the sub-regions depend on L , illustrating the power-law behaviors. However, the intersection coefficients and slopes of the regression lines are not the same, and vary in the ranges $\sim 0.3\text{--}0.5$ and $\sim 0.4\text{--}0.6$, respectively, depending on the sub-region. In general, this could be due to different inclinations as stated above. It also includes the contributions of non-turbulent systematic motions (such as, infall and rotation) to velocity structure of sub-regions.

Furthermore, all of the dependencies lie lower than the Larson’s one. However, for higher lags, the power-law dependence breaks, and the oscillating mode dominates.

If we take the data for the entire filament then the variations in the structure function parameters of the sub-regions are averaged out for compensating individual differences except the global velocity gradient along the filament. In order to examine the influence of global linear gradient to our results, we derived the structure function for the data along the solid curve (see Figure 9a), and compared this result against the structure function computed for the data where linear velocity gradient was subtracted. There are no significant differences found in the parameters of regression lines for lags $\lesssim 3$ pc. For higher lags, any dependence of the structure function on L disappears.

The observed power-law dependence could indicate some general behaviour of the velocity field of the gas in the filament. In particular, it could be a result of the supersonic vortices produced by gas flows along the filament, which dominate at lower lags. At higher lags ($L \gtrsim 2 - 3$ pc), contributions from large-scale and ordered velocity gradients and/or filament fragmentation seem to be dominated. Hence, we could conclude that the value of ~ 3 pc could be an upper scale of the turbulent vortices in the S242 filament. To confirm these conclusions and to further study the properties of turbulence, it is important to derive the structure functions of other molecular clouds and filaments, which will also allow for a comparison.

5. DISCUSSION

In order to understand the physics of filament fragmentation and connection of filaments to star formation mechanisms, *Herschel* sub-mm images in conjunction with observations of molecular line data sets have been employed. Such approach is a powerful tool to assess the ongoing physical processes in the selected target site. To examine the dynamical state of a filament, its observed line mass is compared with the critical line mass, enabling one to infer its stability (e.g., André et al. 2010; Kainulainen et al. 2016; Williams et al. 2018). It has been highlighted in the literature that filaments can collapse longitudinally along their main axis (i.e. global collapse). Two basic types of processes concerning the freefall collapse/global collapse of a uniform-density filament are reported, which are the homologous collapse for the filament with aspect ratio of $A \leq 5$ and the end-dominated collapse for the filament with $A \geq 5$ (e.g., Pon et al. 2012). For filamentary clouds, the aspect ratio is defined as $A = l / R$, where l is the filament’s half-length and R is its radius (see Toalá et al. 2012, for more details). It has also been pointed out that the elongated filaments with large aspect ratios are more prone to end-dominated collapse (e.g., Pon et al. 2012). As mentioned in Introduction, observational examples of end-clumps in isolated filaments are limited (e.g., Zernickel et al. 2013; Beuther et al. 2015; Kainulainen et al. 2016; Hacar et al. 2016).

In Paper I, the selected target S242 filament has been proposed as the end-dominated collapse candidate using the continuum observational data sets. Using the sub-mm images at *Herschel* 500 μm (resolution $\sim 37''$) and *Planck* 850 μm (resolution $\sim 300''$), Figures 12a and 12b

display a large-scale area (~ 102 pc \times 102 pc) containing the site S242 ($^{13}\text{CO } V_{lsr} \sim 0.7$ km s $^{-1}$; Kawamura et al. 1998), respectively. In these figures, two star-forming sites, IRAS 05480+2545 ($^{13}\text{CO } V_{lsr} \sim -9.1$ km s $^{-1}$; Kawamura et al. 1998; Dewangan et al. 2017b) and IRAS 05463+2652 ($^{13}\text{CO } V_{lsr} \sim -10.6$ km s $^{-1}$; Kawamura et al. 1998; Dewangan et al. 2017d), are highlighted by broken circles. Considering the values of $^{13}\text{CO } V_{lsr}$, these two IRAS sites do not appear to be physically connected with the site S242 (see S242 region around $l = 182^\circ.40$; $b = 0^\circ.27$ in Figure 9l in Kawamura et al. 1998). In the dust continuum images, the S242 filamentary structure appears as an isolated molecular cloud (see a rectangle box in Figures 12a and 12b), and its both ends are not linked with the other nearby regions.

With the aid of new OSO-20m molecular (CO and CS) maps, several supersonic molecular sub-regions are identified in the filament (see Section 4.2.1). In Section 4.2.1, with the examination of the dynamical states, the selected sub-regions (except sub-region “2”) in the filament are found to be supercritical, and could not be supported by a combination of thermal and turbulent motions. Furthermore, dense molecular cores are observed mainly toward both the filament ends, and are close to virial equilibrium (see Section 4.2.1 and also Table 2). Additionally, both the ends of the filament contain molecular cores with almost similar masses (see Table 2). In Paper I, the dynamical or expansion age of the S242 H II region was obtained to be $\sim 0.5 - 1.8$ Myr (for $n_0 = 10^3 - 10^4$ cm $^{-3}$). In general, the average lifetime of YSOs (Class I and Class II) can be considered to be $\sim 0.44 - 2$ Myr (e.g., Evans et al. 2009). Clarke & Whitworth (2015) estimated a collapse timescale (t_{col}) for the filamentary structures, which is defined as $t_{col} = (0.49 + 0.26A)/(G\rho)^{1/2}$, where A is the initial aspect ratio of the filament, G is the gravitational constant, and ρ is the volume density of the filament. In the present case, using the molecular line data, the radius, aspect ratio, and density of the filament can be estimated. The observed aspect ratio of the S242 filament is computed to be $A \sim (30 \text{ pc}/2)/(1.5 \text{ pc}/2) \sim 20$. Using a mean density of $n = 10^4$ cm $^{-3}$ (or $\rho = 2.33 \times 1.67 \times 10^{-24} \times 10^4$ gm cm $^{-3}$; see Table 2), we obtain the collapse timescale of $t_{col} \sim 3.5$ Myr, which is much older than the formation of massive stars and clusters of YSOs in the filament. This argument is still acceptable even if we assume about 10–20% error in the above estimates.

The pv plots of molecular lines reveal velocity gradients (~ 1 km s $^{-1}$ pc $^{-1}$) in the direction of both the filament ends. One of the possibilities to explain the observed velocity gradients is star formation activities, while the other explanation of the velocity gradients in the filament is due to the acceleration of the gas. Earlier in the literature, based on the observed velocity gradients along filaments, gas flows along filaments were proposed in both nearby low-mass star-forming clouds (Hacar & Tafalla 2011; Kirk et al. 2013) and massive clouds (Schneider et al. 2010; Peretto et al. 2014; Tackenberg et al. 2014). Furthermore, the oscillatory pattern in velocity is also observed in the velocity space of molecular lines (see also Figure 9). Hacar & Tafalla (2011) observationally studied the filament L1571, and carried out a modelling of velocity oscillations as sinusoidal per-

turbations. They suggested that the observed velocity oscillations along the filament may indicate the filament fragmentation process via accretion along filament. In Section 4.3.2, the structure function in velocity of the filament is derived using the ^{13}CO line data. This analysis indicates that the velocity field in the filament could consist of both turbulent random motions, which dominate on lower- and large-scales, and ordered velocity gradients for $L \gtrsim 2-3$ pc. It also suggests the filament fragmentation, which is probably caused by gravitational contraction/accretion as well as by other feedback effects on the local scale (e.g., ionizing radiation, stellar winds, and star formation activities; Arzoumanian et al. 2013). The differences between power-law dependencies found for various sub-regions of the filament and from the Larson's law could be in general connected with local properties of turbulence in S242. To confirm this conclusion, more data for other objects are needed. Hence, in the case of our selected target, the oscillatory pattern in velocity is suggestive of fragmentation process through accretion along the S242 filament.

Taken together, we find that the observed results of the S242 filament are in agreement with the end-dominated collapse scenario.

6. SUMMARY AND CONCLUSIONS

To understand the physical processes in the S242 filament, we have examined its kinematic structure using CO ($^{13}\text{CO}(1-0)$ and $\text{C}^{18}\text{O}(1-0)$) and CS(2-1) line emission data, which were observed with the OSO-20m telescope. The major results of the present work are as follows:

- The molecular cloud associated with the S242 filament is studied in a velocity range of $[-1, 5]$ km s^{-1} , and its elongated nature (having length ~ 30 pc) is also traced in the molecular maps. One of the filament ends contains the S242 H II region, while the other end hosts several *Planck* cold clumps.
- Several sub-regions are selected in the filament. The values of Mach number (σ_{NT}/c_s) derived using the molecular line data for the sub-regions are computed to be about 2.7–4.0, suggesting these sub-regions are supersonic.
- The observed $M_{\text{line,obs}}$ of the sub-regions (except central part) in the filament are larger than their $M_{\text{line,vir}}$, indicating that these sub-regions (except central part) are supercritical. Hence, the supercritical sub-regions in the filament may not be supported by a combination of thermal and turbulent motions.
- Dense cores are detected in the CS and C^{18}O maps, and are seen mainly toward both the filament ends. These cores are also close to virial equilibrium.
- Mean volume densities of the dense cores at the southern end of the filament are several times higher than those at the northern end. Both the filament ends contain molecular cores with almost similar masses. The filament's collapse time is estimated to be ~ 3.5 Myr.
- Noticeable YSOs are found toward the entire filament, but they are more concentrated toward its ends.
- In the direction of the filament, an oscillatory pattern in velocity is evident, which is indicative of fragmentation. The pv plots of ^{13}CO and C^{18}O reveal velocity gradients ($\sim 1 \text{ km s}^{-1} \text{ pc}^{-1}$) toward both the filament

ends.

- Using the ^{13}CO line, the structure function in velocity of the filament is computed, which is similar as found in the Musca cloud for lags $\sim 1-3$ pc. In the filament, the structure function rises with distance, and shows a power-law behavior (i.e. $\delta V = 0.42 \times L^{0.48}$) at $L \lesssim 3$ pc and an oscillatory pattern at higher L. This dependence lies lower than the Larson's velocity dispersion-size relationship. The oscillatory pattern in velocity at higher lags is suggestive of large-scale and ordered velocity gradients and fragmentation process via accretion along the S242 filament.

All the observational results along with their uncertainties put together, the S242 filament is found to be a reliable candidate of the end-dominated collapse.

We thank the anonymous reviewer for a critical reading of the manuscript and several useful comments and suggestions, which greatly improved the scientific contents of the paper. The research work at Physical Research Laboratory is funded by the Department of Space, Government of India. The OSO-20m observations and data processing were done under support of the Russian Foundation for Basic Research (RFBR) (projects 17-52-45020 and 18-02-0060). The OSO-20m data analysis were done under support of the Russian Science Foundation (project 17-12-01256).

REFERENCES

- André, P., Men'shchikov, A., Bontemps, S., et al. 2010, *A&A*, 518, L102
- André, P., Di Francesco, J., Ward-Thompson, D., et al. 2014, in *Protostars and Planets VI*, ed. H. Beuther et al. (Tucson, AZ; Univ. Arizona Press), 27
- Arzoumanian D., André P., Peretto N., Könyves V., 2013, *A&A*, 553, 119
- Bastien, P. 1983, *A&A*, 119, 109
- Baug, T., Ojha, D. K., Dewangan, L. K., et al. 2015, *MNRAS*, 454, 4335
- Belitsky, V., Lapkin, I., Fredrixon, M., et al. 2015, *A&A*, 580, 29.
- Beuther, H., Ragan, S. E., Johnston, K., et al. 2015, *A&A*, 584, 67
- Blitz, L., Fich, M., & Stark, A. A. 1982, *ApJS*, 49, 183
- Burkert, A., & Hartmann, L. 2004, *ApJ*, 616, 288
- Churchwell, E., Povich, M. S., Allen, D., et al. 2006, *ApJ*, 649, 759
- Churchwell, E., Watson, D. F., Povich, M. S., et al. 2007, *ApJ*, 670, 428
- Clarke, S. D., & Whitworth, A. P. 2015, arXiv:1502.07552
- Condon, J. J., Cotton, W. D., Greisen, E. W., et al. 1998, *AJ*, 115, 1693
- Contreras, Y., Garay, G., Rathborne, J. M., & Sanhueza, P. 2016, *MNRAS*, 456, 2041
- Deharveng, L., Schuller, F., Anderson, L. D., et al. 2010, *A&A*, 523, 6
- Dewangan, L. K., Luna, A., Ojha, D. K., et al. 2015, *ApJ*, 811, 79
- Dewangan, L. K., Ojha, D. K., Luna, A., et al. 2016a, *ApJ*, 819, 66
- Dewangan, L. K., Ojha, D. K., Zinchenko, I., et al. 2016b, *ApJ*, 833, 246
- Dewangan, L. K., Ojha, D. K., Zinchenko, I., Janardhan, P., & Luna, A. 2017a, *ApJ*, 834, 22
- Dewangan, L. K., Ojha, D. K., & Baug, T. 2017b, *ApJ*, 844, 15
- Dewangan, L. K., Baug, T., Ojha, D. K., Janardhan, P., Devaraj, R., & Luna, A. 2017c, *ApJ*, 845, 34
- Dewangan, L. K., Devaraj, R., Baug, T., & Ojha, D. K. 2017d, *ApJ*, 848, 51
- Dewangan, L. K., Ojha, D. K., & Zinchenko, I. 2017e, *ApJ*, 851, 140

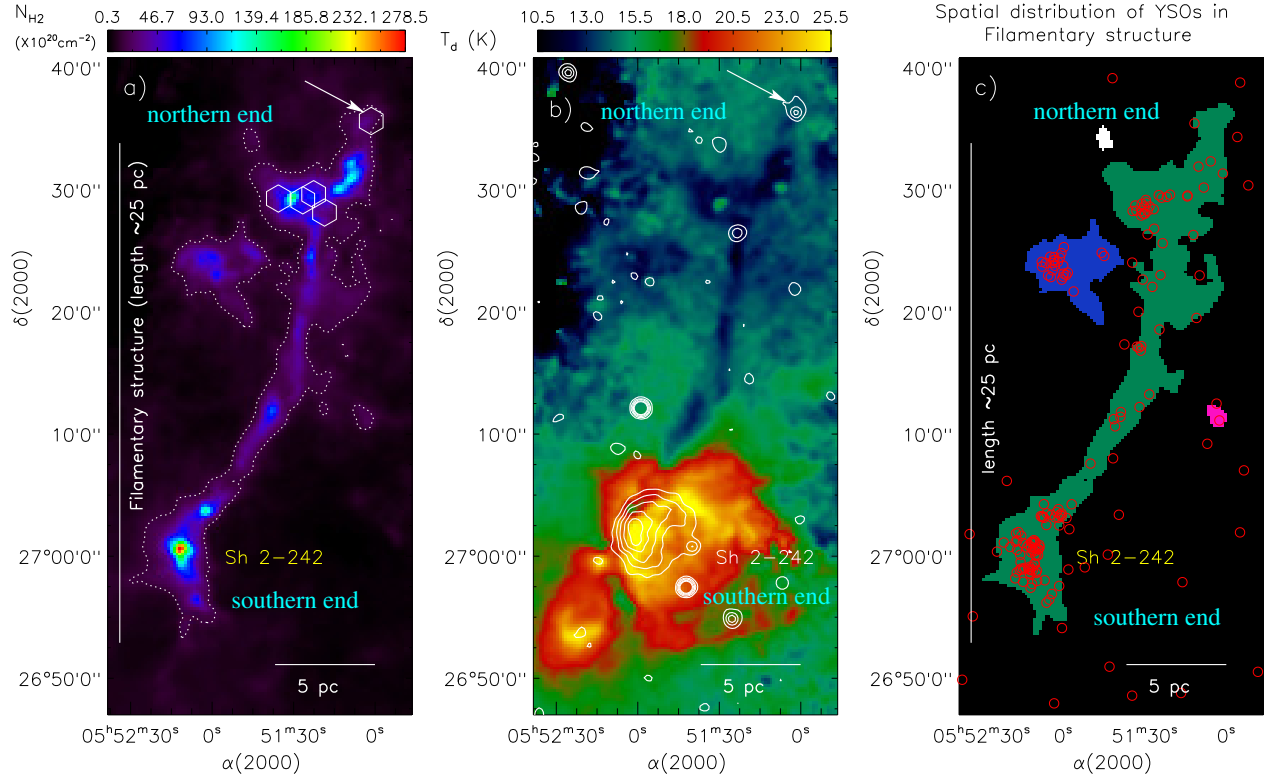


Figure 1. Physical environment of the site S242. a) *Herschel* column density ($N(\text{H}_2)$) map of the region around S242. A filamentary structure is traced in the column density map at a contour level of $1.5 \times 10^{21} \text{ cm}^{-2}$ (see dotted contours). The positions of five PGCCs (e.g., Yuan et al. 2016) are also highlighted by hexagons. An arrow indicates the location of the PGCC G181.84+00.31a1 (e.g., Yuan et al. 2016). b) Overlay of the NVSS 1.4 GHz radio continuum emission contours (in white) on the *Herschel* temperature map. The NVSS 1.4 GHz continuum contours are shown with the levels of $0.45 \text{ mJy/beam} \times [3, 11, 20, 33, 44]$. An arrow indicates the location of the radio continuum source NVSS 055101+273627 (e.g., Condon et al. 1998). c) Spatial distribution of YSOs (see red circles) in the direction of filament as seen in the *Herschel* column density map (see Figure 1a). All these results are taken from Paper I. The scale bar corresponding to 5 pc (at a distance of 2.1 kpc) is shown in each panel.

Evans, N. J., II, Dunham, M. M., Jørgensen, J. K., et al. 2009, *ApJS*, 181, 321
 Frerking, M. A., Langer, W. D., & Wilson, R. W. 1982, *ApJ*, 262, 590
 Hacar, A. & Tafalla, M. 2011, *A&A*, 533, 34
 Hacar, A., Kainulainen, J., Tafalla, M., Beuther, H., & Alves, J. 2016, *A&A*, 587, 97
 Heitsch, F., Hartmann, L. W., Slyz, A. D., Devriendt, J. E.G., & Burkert, A. 2008, *ApJ*, 674, 316
 Heyer, M. H. & Brunt, C. M. 2004, *ApJ*, 615, L45
 Hunter, D. A., & Massey, P. 1990, *AJ*, 99, 846
 Kainulainen J., Hacar A., Alves J., et al., 2016, *A&A*, 586, 27
 Kawamura, A., Onishi, T., Yonekura, Y. 1998, *ApJS*, 117, 387
 Kirk, H., Myers, P. C., Bourke, T. L., et al. 2013, *ApJ*, 766, 115
 Larson, R. B. 1981, *MNRAS*, 194, 809
 MacLaren, I., Richardson, K. M., & Wolfendale, A. W. 1988, *ApJ*, 333, 821
 Mangum, J. G. & Shirley, Y. L. 2016, *PASP*, 128, 9201
 Molinari, S., Swinyard, B., Bally, J., et al. 2010, *A&A*, 518, L100
 Myers, P. C. 2009, *ApJ*, 700, 1609
 Ostriker J., 1964, *ApJ*, 140, 1056
 Planck Collaboration IX. 2014, *A&A*, 571, A9
 Peretto, N., Fuller, G. A., André, P., et al. 2014, *A&A*, 561, A83

Pirogov, L., Zinchenko, I., Caselli, P., et al. 2003, *A&A*, 405, 639
 Pon, A., Johnstone, D., & Heitsch, F. 2011, *ApJ*, 740, 88
 Pon, A., Toalá, J. A., Johnstone, D., et al. 2012, *ApJ*, 756, 145
 Schneider, N., Csengeri, T., Bontemps, S., et al. 2010, *A&A*, 520, A49
 Schneider, N., Csengeri, T., Hennemann, M., et al. 2012, *A&A*, 540, L11
 Snell, R. L., Dickman, R. L., & Huang, Y. L. 1990, *ApJ*, 352, 139
 Solomon, P. M., Rivolo, A. R., Barrett, J., & Yahil, A. 1987, *ApJ*, 319, 730
 Tackenberg, J., Beuther, H., Henning, T., et al. 2014, *A&A*, 565, A101
 Tang, M., Liu, T., Qin, S.-L., et al. 2018, *ApJ*, 856, 141
 Toalá, J. A., Vázquez-Semadeni, E., & Gómez, G. C. 2012, *ApJ*, 744, 190
 Varricatt, W. P., Davis, C. J., Ramsay, S., & Todd, S. P. 2010, *MNRAS*, 404, 661
 Yuan, J., Wu, Y., Liu, T., et al. 2016, *ApJ*, 820, 37
 Wilson, T. L. & Rood, R. 1994, *ARA&A*, 32, 191
 Williams, G. M., Peretto, N., Avison, A., Duarte-Cabral, A., & Fuller, G. A. 2018, *A&A*, 613, 11
 Zernicke, A., Schilke, P., & Smith, R. J. 2013, *A&A*, 554L, 2

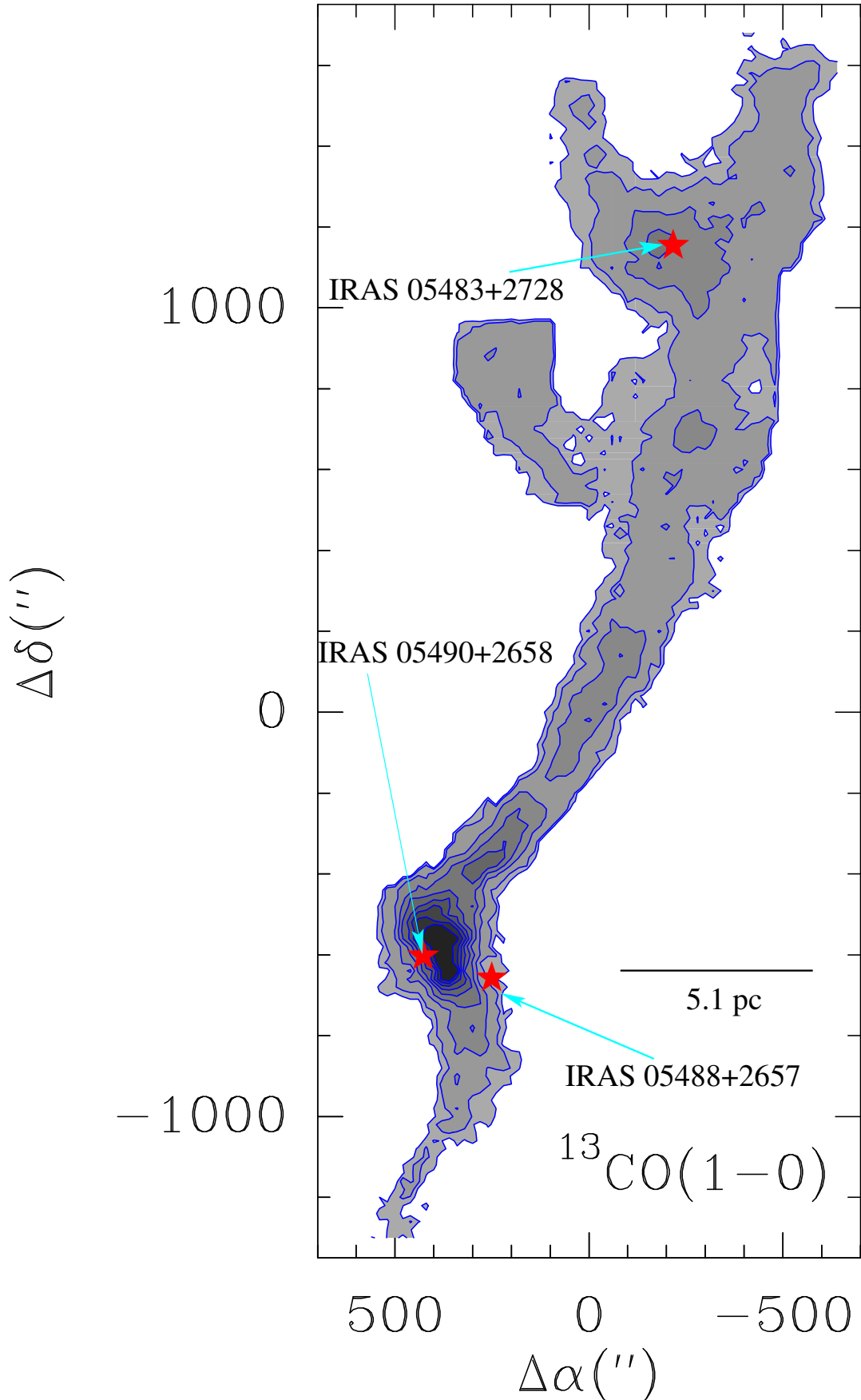


Figure 2. Contour map of the $^{13}\text{CO}(1-0)$ integrated intensity emission in the direction of the site S242. The contours levels (in K km s^{-1}) range from 5 to 40 with a step of 5 with an additional contour of 3 K km s^{-1} . The molecular emission is integrated over a velocity range of $[-12, 6] \text{ km s}^{-1}$. The axes are offsets with respect to a central position (i.e., RA (2000) = $5\text{h } 52\text{m } 12.9\text{s}$; Dec (2000) = $26^\circ 59' 33''$). The positions of IRAS 05490+2658, IRAS 05488+2657, and IRAS 05483+2728 are denoted by stars (in red).

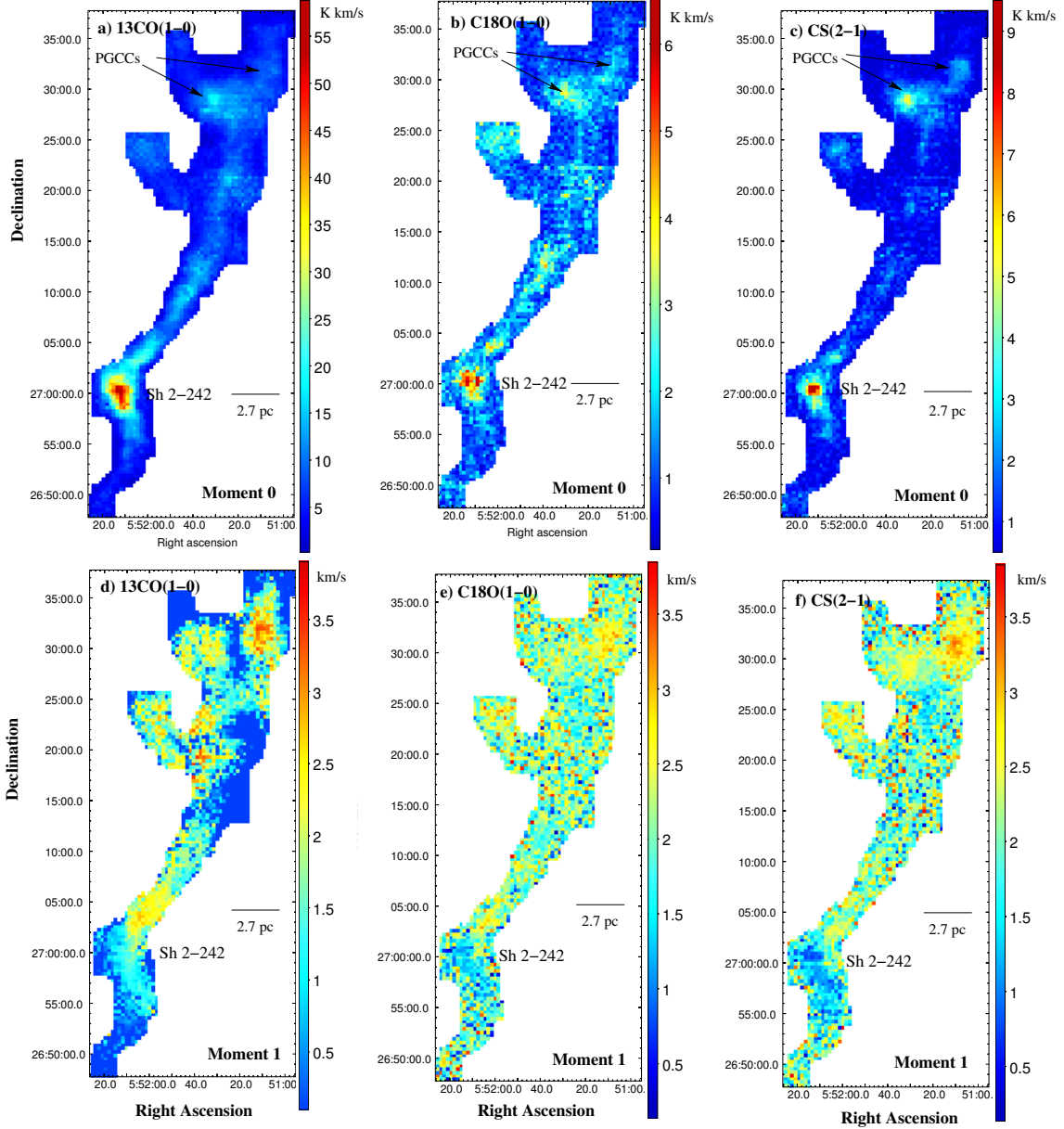


Figure 3. a) The $^{13}\text{CO}(1-0)$ integrated intensity map in the direction of the site S242 (i.e., Moment-0 map). b) Moment-0 map of $\text{C}^{18}\text{O}(1-0)$. c) Moment-0 map of $\text{CS}(2-1)$. d) Moment-1 map of ^{13}CO . e) Moment-1 map of C^{18}O . f) Moment-1 map of $\text{CS}(2-1)$. In all the moment-0 maps, the vertical bar shows the color-coded intensity in K km s^{-1} . In each moment-1 map, the vertical bar shows the color-coded velocity in km s^{-1} .

Table 1

Physical parameters of different molecular sub-regions as highlighted in Figure 6b. Column 1 gives the IDs assigned to the sub-regions. Table also lists length, C^{18}O mass (M_{subreg}), line mass ($M_{\text{line,obs}}$), FWHM ($\text{C}^{18}\text{O } \Delta V$), non-thermal velocity component (σ_{NT}), and critical line mass ($M_{\text{line,vir}}$). These sub-regions are distributed toward the filament.

ID	Length (pc)	$M_{\text{subreg}} (M_{\odot})$	$M_{\text{line,obs}} (M_{\odot}/\text{pc})$	$\Delta V (\text{C}^{18}\text{O}) (\text{km s}^{-1})$	$\sigma_{NT} (\text{km s}^{-1})$	$M_{\text{line,vir}} (\text{at } T = 10 \text{ K}) (M_{\odot}/\text{pc})$
1	9	2353	261	1.48	0.63	192
2	16	3351	209	2.01	0.85	338
3	4.5	957	213	1.22	0.52	135
4	7	1952	279	1.29	0.55	149
5	5	1045	209	1.30	0.55	153

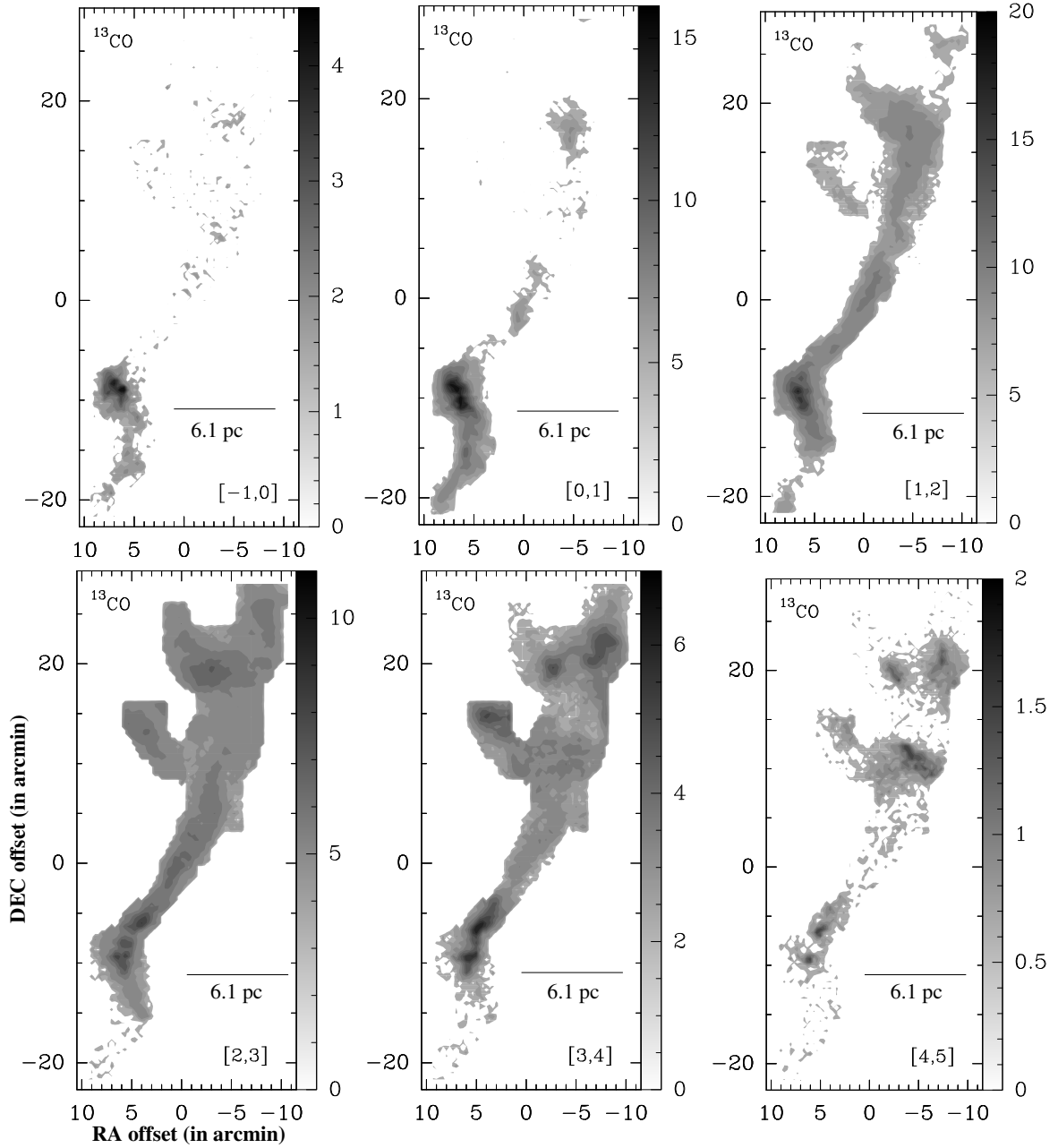


Figure 4. The $^{13}\text{CO}(1-0)$ integrated velocity channel maps (starting from -1 km s^{-1} at intervals of 1 km s^{-1}) in the direction of the site S242. In each panel, the vertical bar shows the color-coded intensity in K km s^{-1} .

Table 2

Five dense cores observed in the CS intensity map (see Figure 6c). Column 1 gives the IDs assigned to cores. Table also lists central positions, CS diameter (D_c), mass derived from C^{18}O (M_c), FWHM (CS ΔV), M_{vir} , and mean number density calculated from M_c and D_c .

ID	RA [2000]	Dec [2000]	D_c (pc)	M_c (M_\odot)	ΔV (km s^{-1})	M_{vir} (M_\odot)	\bar{n} (cm^{-3})
1	5:52:09.3	+27:00:23.3	0.76	295	2.27	409	22500
2	5:52:01.6	+27:03:29.1	0.92	272	2.04	404	11600
3	5:51:32.1	+27:28:55.5	1.33	345	1.53	325	4900
4	5:51:11.6	+27:31:47.9	1.61	250	1.32	295	2010
5	5:51:59.6	+27:23:51.6	1.39	271	1.18	204	3400

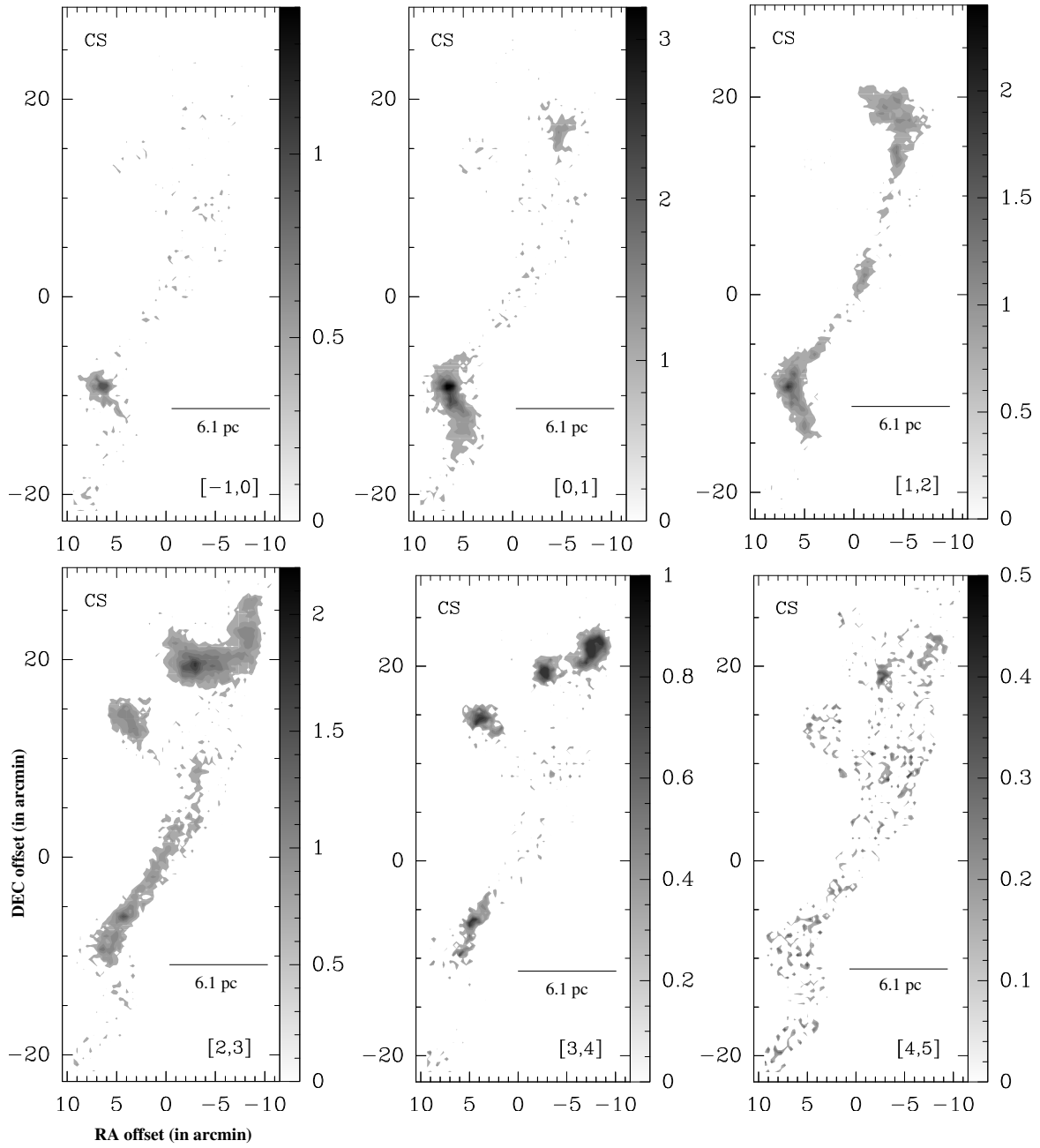


Figure 5. The CS(2-1) integrated velocity channel maps (starting from -1 km s^{-1} at intervals of 1 km s^{-1}) in the direction of the site S242. In each panel, the vertical bar shows the color-coded intensity in K km s^{-1} .

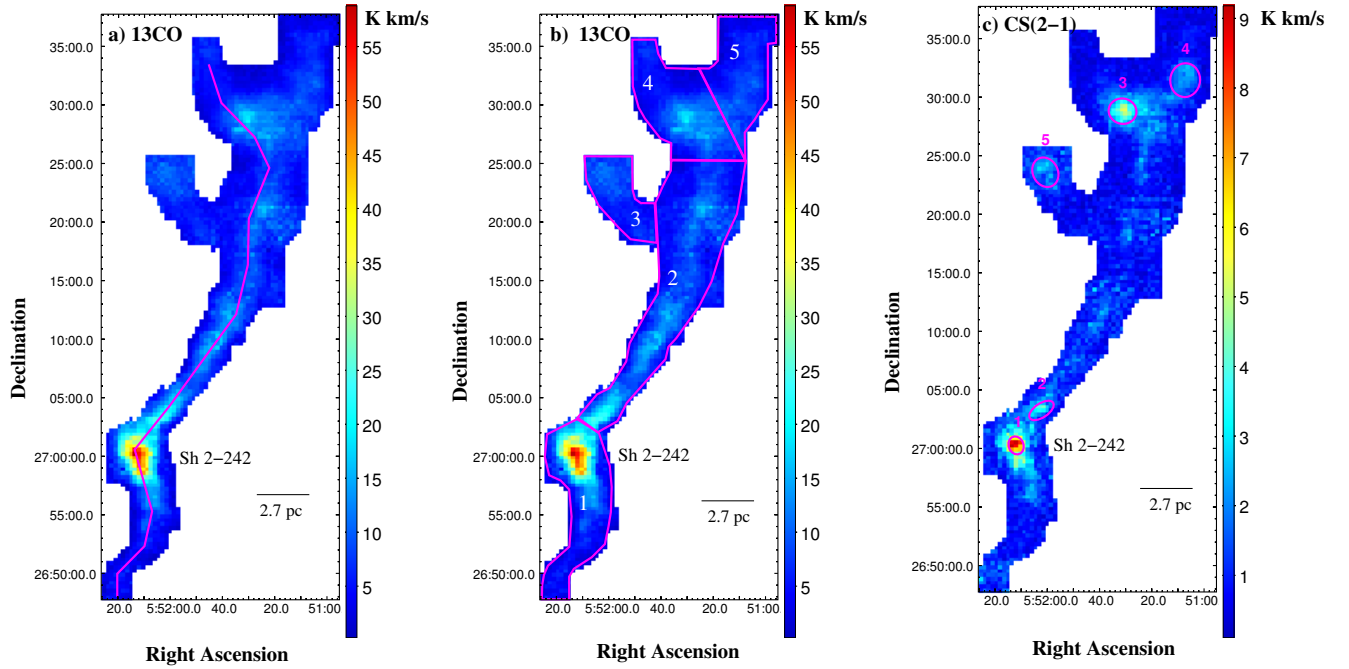


Figure 6. a) Overlay of an arbitrarily chosen solid curve/major axis (in pink) on the map of $^{13}\text{CO}(1-0)$ integrated intensity, where position-velocity plots are calculated (see Figures 7a, 7b, and 9). b) Overlay of different sub-regions on the map of $^{13}\text{CO}(1-0)$ integrated intensity, where masses are estimated (see Table 1). c) Five dense cores highlighted in the map of $\text{CS}(2-1)$ integrated intensity (see ellipses). In each panel, the vertical bar at the right shows the color-coded intensity in K km s^{-1} .

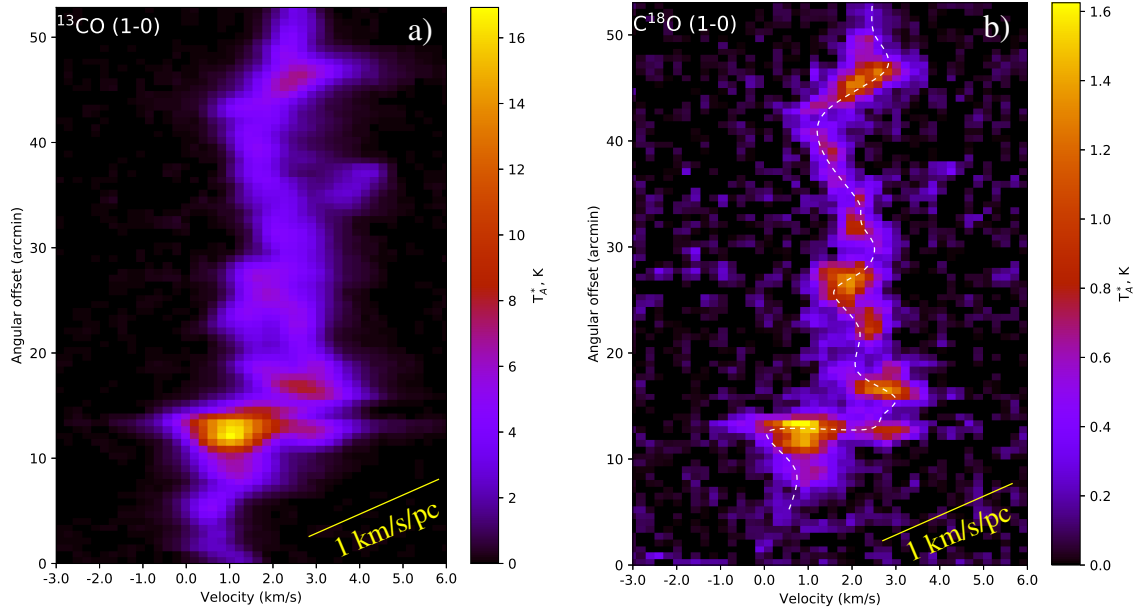


Figure 7. a) The $^{13}\text{CO}(1-0)$ position-velocity plot. Antenna temperatures are shown in colors, and represent the averaged values for the bins with dimensions $40'' \times 120''$ along a solid curve shown in Figure 6a. b) Same as Figure 7a, but for $\text{C}^{18}\text{O}(1-0)$. An arbitrarily chosen dashed curve (in white) shows an oscillatory-like velocity pattern along the filamentary structure. A scale bar corresponding to $1 \text{ km s}^{-1} \text{ pc}^{-1}$ is shown in each panel.

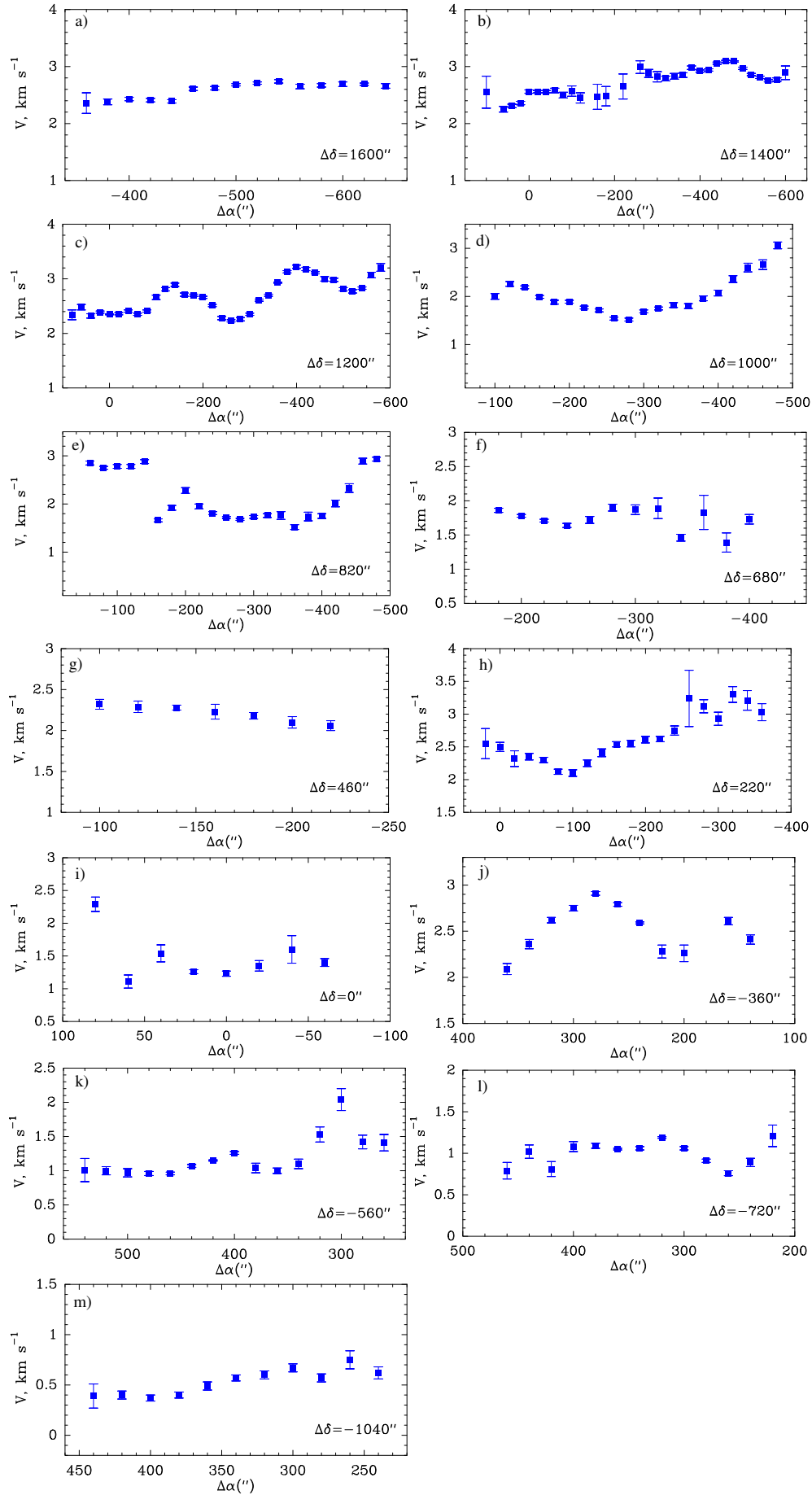


Figure 8. Plots of velocity scans perpendicular to the filament for different $\Delta\delta$ values (see Figure 2). In each panel, the separation of $100''$ corresponds to 1 pc (at a distance of 2.1 kpc).

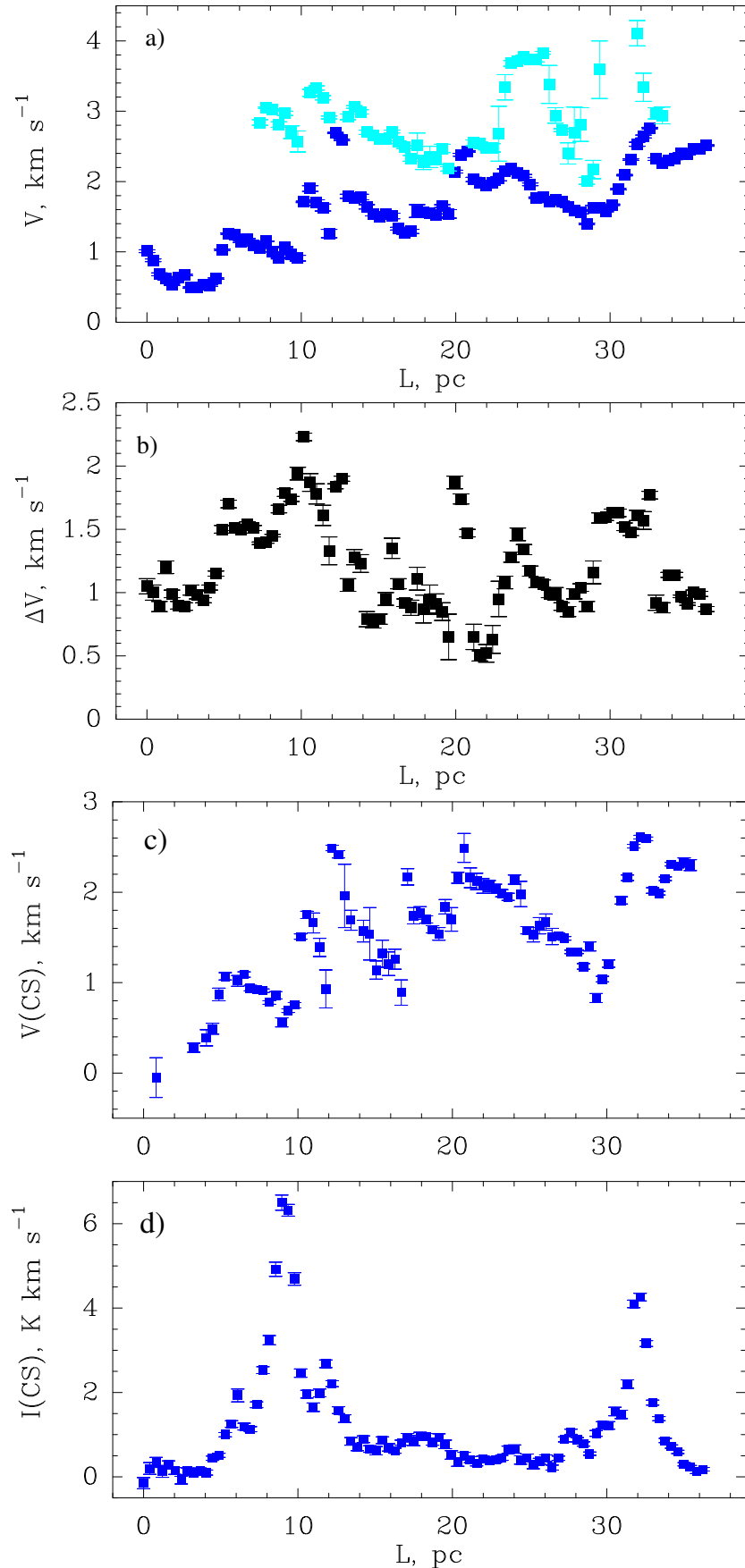


Figure 9. a) The variation of $^{13}\text{CO } V_{lsr}$ along the filament (see a solid curve in Figure 6a). Both the main V_{lsr} (dark blue) and the second V_{lsr} component (light blue) are presented against the length. b) Same as Figure 9a, but for $^{13}\text{CO } \Delta V$ (i.e. FWHM of the main component). c) The variation of $\text{CS}(2-1) V_{lsr}$ along the filament (see a solid curve in Figure 6a). d) The variation of $\text{CS}(2-1)$ integrated intensity along the filament. In each panel, all the points are obtained from the averaging of 9 spectra over the same bins. In the panels “c” and “d”, each data point is obtained from the $\text{CS}(2-1)$ spectra, which are averaged over the bin with dimensions of $60'' \times 60''$.

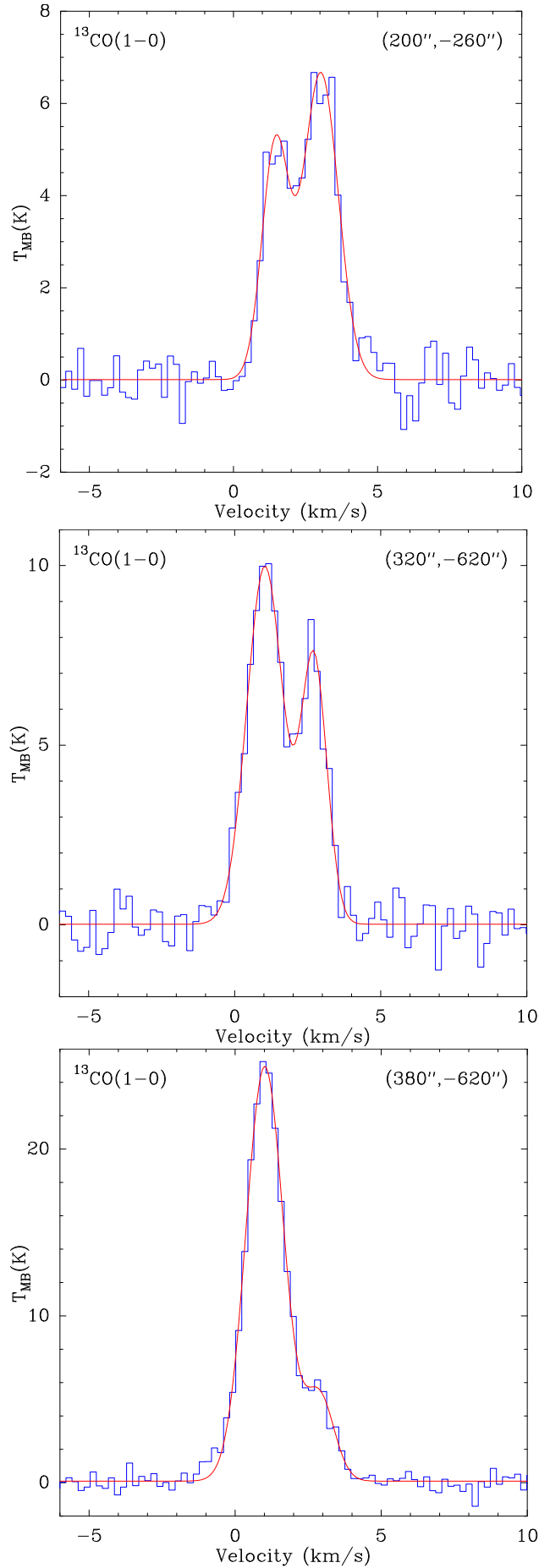


Figure 10. Two-component ^{13}CO spectra at different positions (see also Figure 2). The position offsets are marked at top right in all the panels. In each panel, the observed spectrum is overlaid with the Gaussian fit.

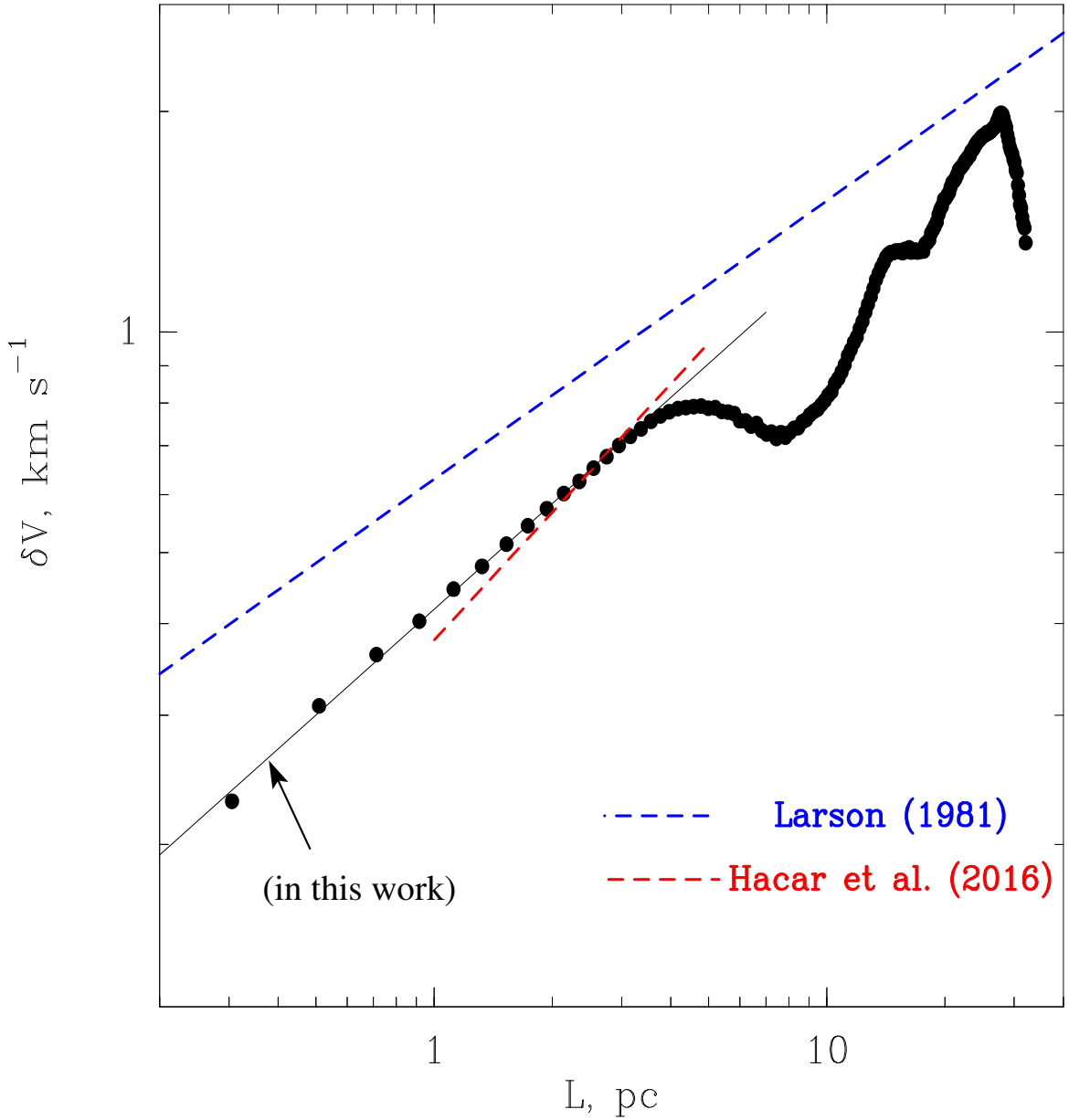


Figure 11. Structure function in velocity δV as a function of length (i.e. lag) derived from the ^{13}CO line data. The structure function is derived using the total data set. The Larson’s velocity dispersion-size relationship (i.e. $\delta V = 0.63 \times L^{0.38}$) is also marked by a broken blue line. The velocity dispersion-size relationship of the Musca cloud is also shown by a broken red line (e.g., $\delta V = 0.38 \times L^{0.58}$; Hacar et al. 2016). In the filament, a linear relation is found between $\log(\delta V)$ and $\log(L)$ for $L \lesssim 3$ pc, where $\delta V = 0.42 \times L^{0.48}$ (see a solid black line in the figure and also text for more details). The errors in the intersection coefficient and the slope are ~ 0.003 and ~ 0.01 , respectively.

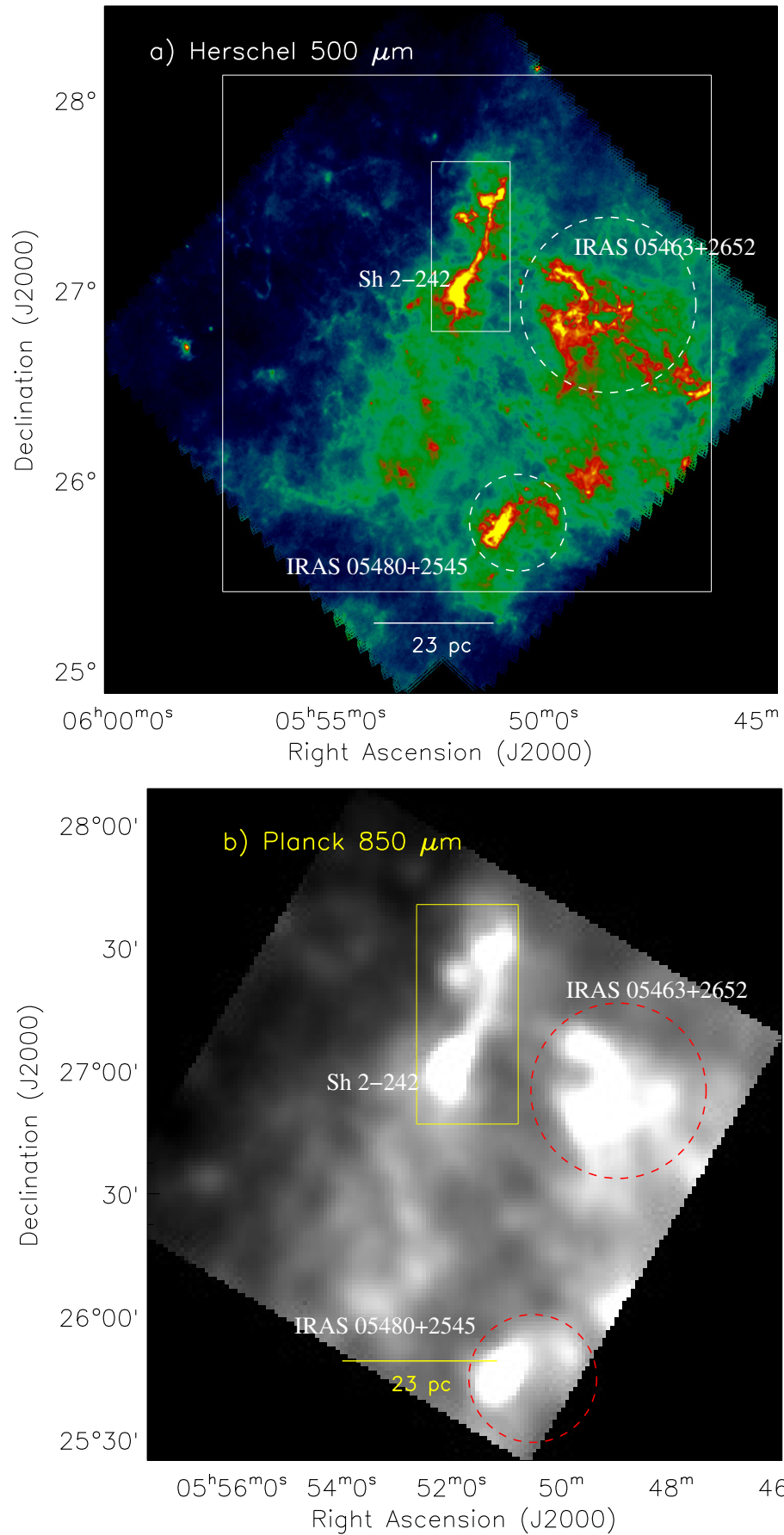


Figure 12. Large-scale image of a field hosting the site S242. a) False color *Herschel* image at 500 μm . The square box highlights an area of $2^\circ.8 \times 2^\circ.8$ (or $102.6 \text{ pc} \times 102.6 \text{ pc}$). b) Grey-scale color *Planck* image at 850 μm (see a square box in Figure 12a). In each panel, a rectangle box indicates the area shown in Figure 1, and also highlights the location of the S242 filament. In both the panels, broken circles show the star-forming sites IRAS 05480+2545 (Dewangan et al. 2017b) and IRAS 05463+2652 (Dewangan et al. 2017d).